High field hybrid photoinjector electron source for advanced light source applications

L. Faillace[1,2,*] R. Agustsson,[3] M. Behtouei,[1] F. Bosco,[2,4] D. Bruhwiler,[5] O. Camacho,[6]
M. Carillo,[2,4] A. Fukasawa,[6] I. Gadjev,[3] A. Giribono,[1] L. Giuliano,[2,4] S. Kutsaev,[3]
N. Majernik,[6] M. Migliorati,[2,4] A. Mostacci,[2,4] A. Murokh,[3] L. Palumbo,[2,4] B. Spataro,[1]
S. Tantawi,[7] C. Vaccarezza,[1] O. Williams,[6] and J. B. Rosenzweig[2,6]

[1]*INFN—Laboratori Nazionali di Frascati, Via E. Fermi 54, Frascati (Roma) 00044, Italy*
[2]*Sapienza University, Department of Basic and Applied Sciences for Engineering,*
via A. Scarpa 14, 00161 Roma, Italy
[3]*RadiaBeam Technologies LLC, 1717 Stewart Street, Santa Monica, California 90404, USA*
[4]*INFN—Sezione di Roma, P.le Aldo Moro 2, Roma 00185, Italy*
[5]*RadiaSoft LLC, 6525 Gunpark Dr, Boulder, Colorado 80301, USA*
[6]*University of California, Department of Physics and Astronomy, 405 Hilgard Avenue,*
Los Angeles, California 90095, USA
[7]*SLAC National Accelerator Laboratory, Menlo Park, California 94025, USA*

The production of high spectral brilliance radiation from electron beam sources depends critically on the electron beam qualities. One must obtain very high electron beam brightness, implying simultaneous high peak current and low emittance. These attributes are enabled through the use of very high field acceleration in a radio-frequency (rf) photoinjector source. Despite the high fields currently utilized, there is a limit on the achievable peak current in high brightness operation, in the range of tens of Ampere. This limitation can be overcome by the use of a hybrid standing wave/traveling wave structure; the standing wave portion provides acceleration at a high field from the photocathode, while the traveling wave part yields strong velocity bunching. This approach is explored here in a C-band scenario, at field strengths (>100 MV/m) at the current state-of-the-art. It is found that one may arrive at an electron beam with many hundreds of Amperes with well-sub-micron normalized emittance. This extremely compact injector system also possesses attractive simplification of the rf distribution system by eliminating the need for an rf circulator. We explore the use of this device in a compact 400 MeV-class source, driving both inverse Compton scattering and free-electron laser radiation sources with unique, attractive properties.

I. INTRODUCTION

High brightness beams, characterized by high peak currents and ultralow normalized emittances, are of fundamental importance in new linear accelerator-based facilities for numerous applications, such as electron-positron or photon-photon colliders [1,2], x-ray free-electron lasers [3], wakefield accelerator experimentation, coherent THz, and inverse Compton scattering x-ray or γ-ray sources [4]. Other important applications can be found, for example, in the field of biomedical science, where low emittance photon beams are used to obtain high quality images for diagnostics due to the increased resolution and contrast they can provide [5,6].

For electron beams, in order to obtain high brightness, photoinjectors [7–9] have been the essential instrument in worldwide use for the last three decades. Their common initiation point for giving birth to the electron beam is a photocathode surface, which, after being illuminated by a femtosecond-to-picosecond laser, typically in the ultraviolet spectral region, emits electron bunches by the photoelectric effect.

As of today, three types of photoinjectors are nowadays employed in laboratories worldwide: the dc photoinjector (dc gun), the normal conducting radio-frequency (rf) photoinjector (NCRF gun), and the superconducting rf photoinjector (SRF gun). The choice of a specific technology depends on many factors such as the peak electric field, beam energy, and average current. dc guns are limited in the maximum electric field strength that can be applied at

*Corresponding author.
luigi.faillace@lnf.infn.it

the cathode surface (of the order of 10 MV/m) and the maximum output beam energy, due to the short accelerating gap. Therefore, the beam quality in terms of brightness (i.e., high bunch charge and small transverse emittance) is not attainable in a compact footprint [10–14]. SCRF guns are suitable for high repetition rate operation (even beyond 1 MHz) and have low electric fields at the cathode (of the order of 10 MV/m), leading to an electron beam with large transverse emittance, as of today [15–17]. On the other hand, NCRF photoinjectors, operated in pulsed mode, with metallic cathodes made of bulk material can sustain electric fields well above 100 MV/m (at the cost of a lower duty cycle, typically around 100 Hz repetition rate), thus producing high-brightness electron beams. Their volumetric footprint is a few tens of cubic centimeters, thus their compactness [18–22]. Moreover, it has been recently suggested the possibility of achieving surface fields around 500 MV/m. In support of this, experimental results have been recently obtained in cryogenically cooled NCRF accelerating structures [9,23]. Cryogenics operation (e.g., with liquid nitrogen at 77 K or 45 K [24] is also a valid compromise between the other NC and SC technologies. In fact, there is no need for an expensive and complicated cryogenic plant since the accelerating cavity can be directly placed inside a vacuum cryostat and cooled by a pulse tube cryocooler's cold head. To the same category belong those guns which are operated in a quasi-CW mode, i.e., at very high repetition rates (in the MHz or GHz range), although their footprints are quite large because of the necessity to dissipate high-average dissipated rf power [25,26].

In order to produce a high peak current ($\gg$100 A) and low-emittance (<1 μm) electron beam, our proposal stands in the rf and beam dynamics design of an ultracompact NRCF photoinjector in C-band of 4–5 MeV output energy, with a hybrid configuration that can be installed in a few tens of centimeters.

The photocathode is embedded in a standing wave (SW) radio-frequency (rf) structure which accelerates the beam up to an energy of few MeV (typically 4–5 MeV) in a few cavity cells. This first part of the photoinjector is traditionally referred to as the rf gun and is typically separated from the downstream postacceleration linac, as is employed in all but the lowest energy experiments. After the exit of the gun, the beam ballistically propagates through a drift (with a consequent bunch lengthening) before entering a linac, which is often chosen as a traveling wave (TW) type. This linac is used for further acceleration or for other rf manipulations. For example, one may utilize velocity bunching compression and rf transverse focusing to optimize the brightness [27,28] by increasing the current and/or decreasing the emittance. The rf input power into the gun and the linac can be fed with two independent power sources, or by a single klystron, with the use of a power splitter. In both cases, however, a circulator is typically necessary. It is often located upstream of the SW rf gun in

the waveguide network, in order to protect the power source from reflections due to mismatch upon filling and emptying the SW cavity.

A different concept for obtaining high brightness beams has been introduced in the form of a *hybrid* rf photoinjector. The device is an integrated structure consisting of a photocathode embedded in an initial 2.5 gun cell SW section which is connected through an input coupling cell directly to a TW section. This configuration offers several advantages over the standard split SW/TW system, in both rf engineering and beam physics performance. In particular, the design nearly eliminates rf reflections from the SW section, thus obviating the use of a circulator. Moreover, since the cell that couples the two structures replaces the long beam pipe and the matching section following the rf gun, one avoids the bunch lengthening effect due to the ballistic drift. On the contrary, the rf coupling between the SW and the TW sections optimally results in a 90° phase shift of the accelerating field, with a consequent strong velocity bunching effect applied to the beam. This effect can be used to produce very short bunch lengths, over an order of magnitude smaller than that obtained in a split configuration. Additionally, these properties, because of the modest normalized vector potential ($\alpha_{\rm rf} = eE_{acc}/m_e c \omega_{\rm rf}$) [29] involved, permit higher frequency (at high field [30]) operation. This can dramatically improve the beam brightness with economic use of rf power.

The rf design of an S-band hybrid photoinjector was discussed in [31] in the context of a UCLA/INFN-LNF collaboration, while the first realization, including high-power tests and measurements, was carried out at Pegasus Lab, UCLA [32,33], by feeding the structure with a klystron with an rf power of 11.5 MW. The possibility of a straightforward scaling implementation of the structure to higher frequencies was analyzed in [34], and this led to the X-band version rf design and realization [35], as well as beam dynamics studies and applications enabled [36]. As the X-band case presented technical challenges—neither the scaling of the solenoid nor cavity fields are straightforward—the realization of the device to 11.424 GHz was not fully carried out. Indeed, if one wishes to operate at field values inside of the current state-of-the-art, then C-band presents an achievable choice.

As such, in this paper, we present the design of a hybrid photoinjector operating at 5.712 GHz. This solution has some advantages with respect to the S-band and X-band devices. The higher frequency with respect to S-band makes it more compact at equivalent energies and allows one to obtain higher brightness beams since this quantity is proportional to λ^{-2} using natural scaling [30,37]. On the other hand, the lower frequency with respect to X-band reduces the overall costs, in particular, the rf power source. Moreover, the largest irises of the rf cavities facilitate the beam transport and reduce the deleterious effect of wakefields—beam loading and beam breakup (BBU) [38–40].
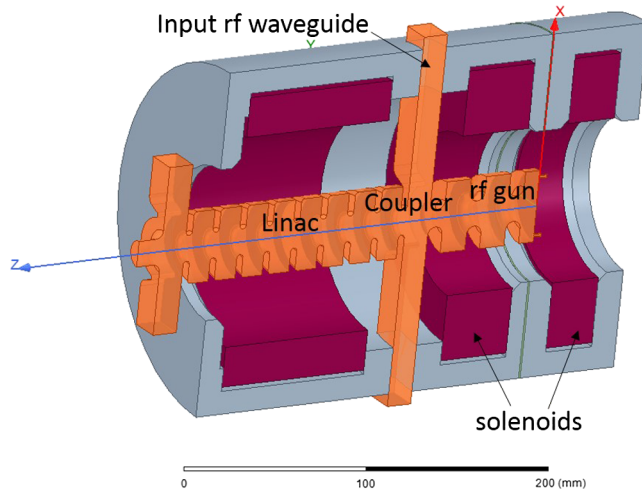
FIG. 1. Basic layout of the compact hybrid C-band photoinjector.

The basic layout of our proposed design is shown in Fig. 1. Starting from the rhs, we show the SW rf gun, then the coupling cell with the input rf waveguide, and finally the TW section. The rf structure is enveloped by the solenoid coils and yoke assembly—this supplies a magnetic field to focus the beam and allow optimization of the emittance compensation.

The paper is organized as follows: In the following section, we present the rf design of the hybrid structure, with the management of fields and power distribution. Then, in Sec. III, the beam dynamics performance is discussed, showing, for the first time for this class of photoinjectors, the entire optimization process of the emittance compensation in the presence of strong longitudinal bunching. In the following two sections, a thorough study of the beam in the drift following the photoinjector, including a discussion of the emittance oscillations, space charge modeling, and slice analysis is performed. The SW linac provides acceleration to reach above 400 MeV, with the beam dynamics presented in Sec. V. The applications of this injector system, in particular the case for driving an inverse Compton scattering source and a short wavelength FEL source, are explored in Sec. VI. A final summary section is dedicated to conclusions and outlook for the future.

II. HYBRID STRUCTURE rf DESIGN

The rf design of the compact C-band hybrid photoinjector was carried out using the electromagnetic simulations code HFSS [41] and was initially introduced in [42]. A one-quarter section of the C-band hybrid photoinjector from the HFSS analysis is shown in Fig. 2. The SW section is composed of two-and-a-half cells operating in the π mode. The TW section design employs the $2\pi/3$ mode. The structure is optimized in order to obtain an electric peak
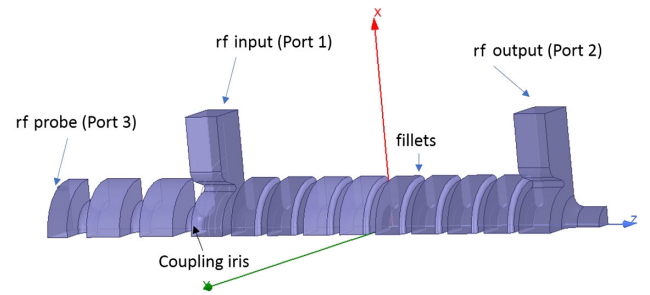

FIG. 2. One-quarter section of the C-band hybrid photoinjector from HFSS.

field at the cathode of 120 MV/m. In this hybrid configuration, the initial rf mismatch is reduced, which means low reflected power from the structure to the source. The rf power is provided through a symmetrical dual-feed waveguide system which is visible in Fig. 1 from the 3D rendering while in Fig. 2 only one-quarter of the structure, used for rf simulations, is shown because of its symmetry. The employing of a symmetrical feeding power avoids both field phase and amplitude asymmetries. In this configuration, there is no need for a high-power circulator. As a result, the rf power network and accelerator system footprint are considerably reduced.

The on-axis accelerating electric field can be expressed as follows:

$$E_z(z, t) = E_0(z) \cos(\varphi(z) + \omega t), \tag{1}$$

where $E_0(z)$ is the on-axis field amplitude and $\varphi(z)$ is the field phase.

The on-axis electric field amplitude profile and phase distribution are shown in Figs. 3 and 4, respectively. The $\pi/2$ phase-shift between the SW and TW section, a particular feature of this hybrid structure, allows for velocity bunching thus obtaining ultrashort beams.

The main rf parameters are given in Table I. The required rf input power is about 40 MW in order to obtain a peak surface electric field at the cathode equal to 120 MV/m. The ratio between the SW on-axis peak
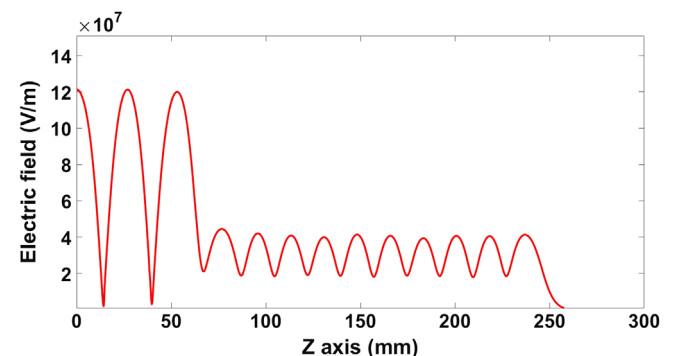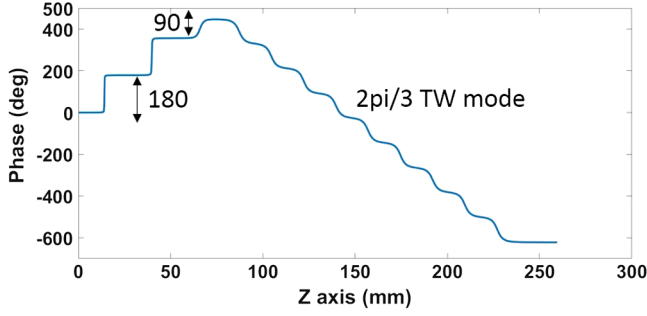

FIG. 3. On-axis electric field amplitude profile.

FIG. 4.   On-axis electric field phase distribution.

electric field and the average TW electric field is equal to $E_{z,p,SW}/\langle E_{z,TW}\rangle = 3.25$, where $E_{z,p,SW}$ is also the maximum field value E_{max} of the on-axis accelerating electric field.

A. TW section rf efficiency optimization

In order to improve the power efficiency of the hybrid photoinjector, we have also investigated a tapered TW section. Smaller group velocity at TW input allows a larger field in the SW section enhancing the energy with less available power. It was possible to reduce rf input power to about 20 MW versus the 40 MW required for the original design. As a consequence, the bunching effect becomes weaker. The outcome offers a solution that overcomes possible limitations in the rf power source at the expense of the output minimum bunch length achievable, i.e., and the associated maximum available bunch peak current, as discussed in the following section.

For a Compton scattering source, as is shown throughout this work, the scenario with higher efficiency and lower peak current can fulfill the design specifications. For the short wavelength FEL case, however, we have investigated the use of the original design with more effective bunching, which uniquely enables the gain needed for this application.

III. BEAM DYNAMICS

In this section, we discuss the optimization of the emittance compensation process for this new class of

TABLE I.   Main rf parameters for an rf input power $P_{rf} = 40$ MW and cathode electric field $E_z = 120$ MV/m.

Parameter	SW section	TW section
Operation mode	π	$2\pi/3$
Quality factor, Q	9900	9900
Effective shunt impedance, R_{sh}	52 MΩ/m	65 MΩ/m
Mode separation	21.5 MHz	40 MHz
Buildup time, τ	530 ns	$\cdots$
Group velocity, v_g	$\cdots$	2.73%
Attenuation, α	$\cdots$	0.23 m^{-1}
Filling time, t_f	$\cdots$	21.3 ns

TABLE II.   Main input electron beam parameters.

Parameter	Value
Beam charge, Q	250 pC
Spot size, $\sigma_{x,y}$ (cut at 1σ)	0.5 mm
Bunch length, σ_z	0.5 ps
E field at cathode, E_0	120 MV/m
Number of macroparticles	50 000

photoinjectors. This is a new design horizon, given the use of 2.5 accelerating cells, a scenario not previously presented.

The beam dynamics of the C-band photoinjector was performed by using the General Particle Tracer (GPT) code [43]. The main input electron beam parameters at the extraction plane (photocathode) are given in Table II. The beam charge is $Q = 250$ pC, which is attractive for the radiation production applications we are examining. The first design explorations were performed with a uniform beam transverse profile; however, a collimated distribution, formed with a Gaussian profile cutoff at 1σ, with an rms spot size $\sigma_{x,y} = 500$ μm is ultimately chosen. The rationale for this choice is discussed below. The bunch length is also Gaussian in profile with $\sigma_z = 0.5$ ps.

The on-axis normalized magnetic field profile is given in Fig. 5. The optimal peak magnetic field of the solenoid around the hybrid structure is $B_z = 0.27$ T. The amplitude of the $E_{zp,SW}/\langle E_{z,TW}\rangle$ accelerating fields and the solenoid field in the SW and TW sections ($B_{z,SW}$ and $\langle B_{z,TW}\rangle$, respectively) and the laser input phase are optimized to maximize the beam brightness after the end of the structure, with subsequent completion of the simultaneous compression and emittance compensation processes. A full engineering design of this relatively modest field (particularly as compared with the previous attempt at designing an X-band hybrid, for which the solenoid was extremely challenging) has been completed and is presently being constructed. In this design, a bucking coil is used to cancel the magnetic field at the cathode, eliminating contributions to the emittance from the electrons' canonical angular momenta.
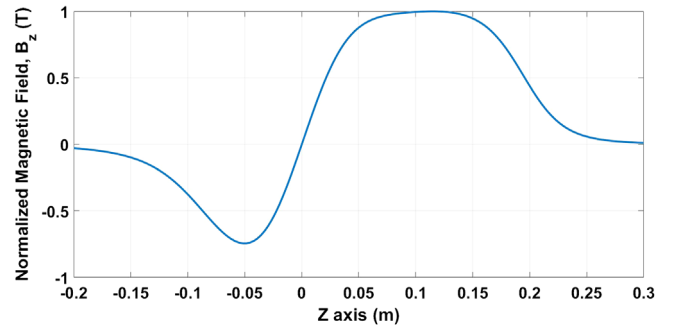

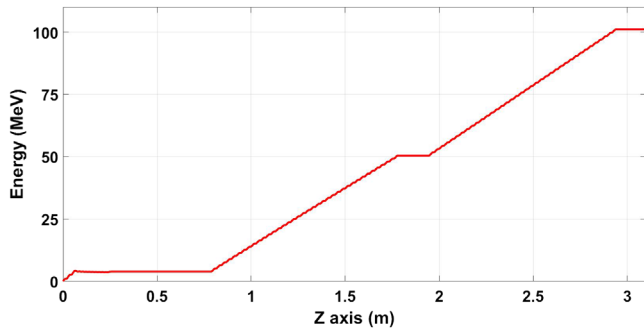FIG. 5.   On-axis normalized magnetic field profile.

FIG. 6. The beam energy gain from the cathode at $z = 0$ m up to the end of the beamline with two high-gradient linacs.

FIG. 8. Evolution of the rms bunch length σ_z along the beamline; beam charge 250 pC, energy 100 MeV.

In order to attain the emittance compensation process, as a first attempt, two linacs based on a distributed-coupling geometry due to Tantawi [44], operated near 50 MeV/m accelerating gradient, are used. The first linac entrance is located at 80 cm from the hybrid photoinjector. The beam energy reaches over 100 MeV after the linac sections, as illustrated in Fig. 6. We note that this energy corresponds to a maximum needed for demonstration experiments using Compton x rays in the injector project's initial phase; the full system energy for second phase production of γ rays has been also simulated, and its details will be reviewed in a separate document.

All parameters were optimized in order to minimize the beam emittance, which reached below $\epsilon_n = 0.5$ mm mrad, while maintaining strong pulse compression downstream of the hybrid. The emittance performance obtained is shown in the simulations displayed in Fig. 7. In the same figure, we show the beam transverse distribution, which follows the predicted ponderomotive focusing in axisymmetric linacs [45], with a final spot size of about $\sigma_{x,y} = 200 \ \mu$m. This ultimately led to a condition just upstream of the linac entrance where there are nearly simultaneous longitudinal and transverse space-charge dominated waists.
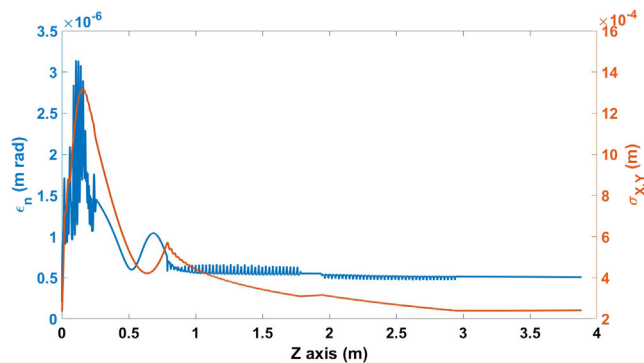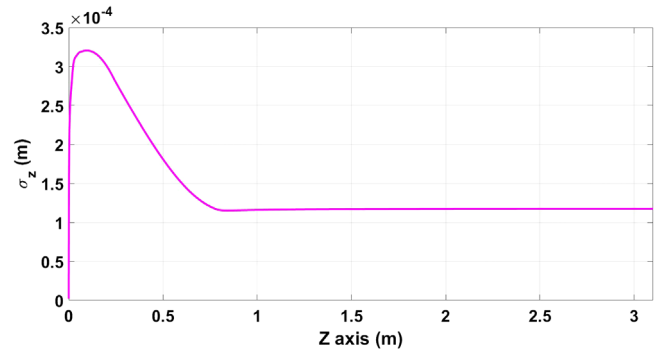
It is noted that the beam envelope in the linac evolves as $\sigma_{x,y}(z) \propto \gamma^{-1/2}$, obeying the prediction behavior for an optimally emittance-compensated beam [37] by following the *invariant envelope*. The longitudinal waist approximately yields the final bunch length, as the linac acceleration freezes out further evolution of σ_z, which reaches 400 fs (see Fig. 8). This corresponds to a beam peak current above 300 A. This scenario results in the 6D phase space (on both the transverse and longitudinal planes) compensation, in which minima in beam emittances (as well as sizes) are reached in all three phase planes. The detailed analysis of this joint transverse and longitudinal waist, which occurs nearly simultaneously in z, is carried out in a following section utilizing the beam slice investigation.

This short bunch length provides an essential advantage in Compton scattering sources, as it adds flexibility in introducing a small crossing angle in the interaction without diminishing the scattered photon production. It is also a key enabling characteristic for driving a compact, short wavelength free-electron laser. In both Compton scattering sources, the low emittance enables a desired narrow bandwidth in the scattered photon flux, whereas in the FEL, the low emittance and high peak current yield high gain in a short period undulator.

A. Laser pulse shaping

Beam shaping at the photocathode injection has been investigated with two different transverse laser distributions assumed. The first form is a simple uniform distribution in r (flattop), while the second has the shape of a truncated (at 1σ) Gaussian. Both distributions have a hard radial edge obtained by collimation at a radius of 0.5 mm. These two cases are compared in Fig. 9. The results of this study demonstrated that the choice of the transverse truncated Gaussian gives two major operational advantages, as theoretically described and experimentally observed in various rf gun-based sources [46–48]. First, in a practical concern, it reduces the complexity of the drive laser optical system, as the flattop is more challenging to obtain while maintaining good laser system efficiency. Second, it yields

FIG. 7. Evolution of the rms transverse beam size $\sigma_{x,y}$ and normalized transverse emittance ϵ_n along the beamline; beam charge 250 pC, energy 100 MeV.
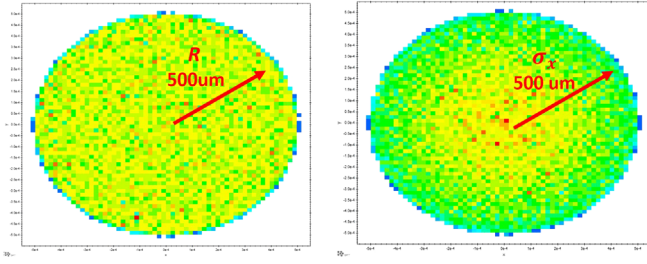
FIG. 9.   (left) Flattop profile in x and y; (right) cut-Gaussian of same radius (0.5 mm) which corresponds to 1σ in the distribution before the cut.

(a) Transverse (red) and longitudinal (blue) rms envelope

a notable increase of brightness in the electron beam through improvement in the collective beam dynamics.

Indeed, the most critical advantage of using this highly optimized source is that the emittance is lowered significantly as compared to previous designs. In initial studies using a uniform transverse laser illumination, the optimized rms normalized emittance has been found to be near 0.75 mm mrad. When one uses the truncated Gaussian laser profile on the photocathode, however, this normalized emittance descends dramatically, to 0.46 mm mrad. The simulation of this case, which is performed using 1 million superparticles for convergence to definitive results, is shown in Fig. 10.

This improvement can be ascribed to the fact that the initial beam dynamics is dominated by rapid expansion, first longitudinally and then transversely. This scenario may therefore be described as a mixed longitudinal-transverse blowout mode. In this way, as discussed in further detail below, the effects of space charge tend to produce a uniform ellipsoidal beam distribution in configuration space at minimal cost in initial emittance growth.
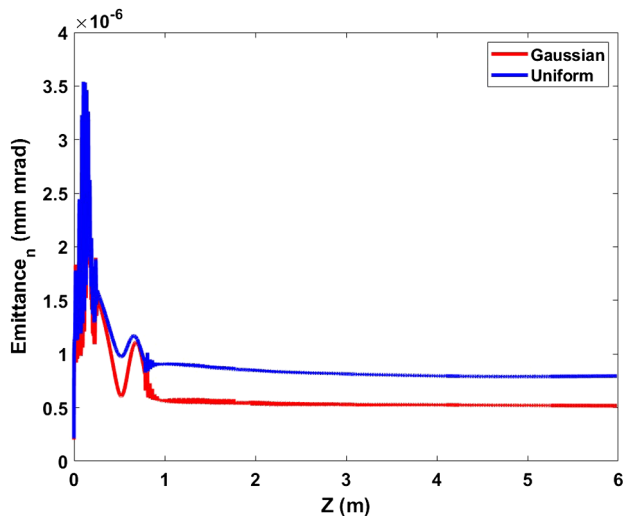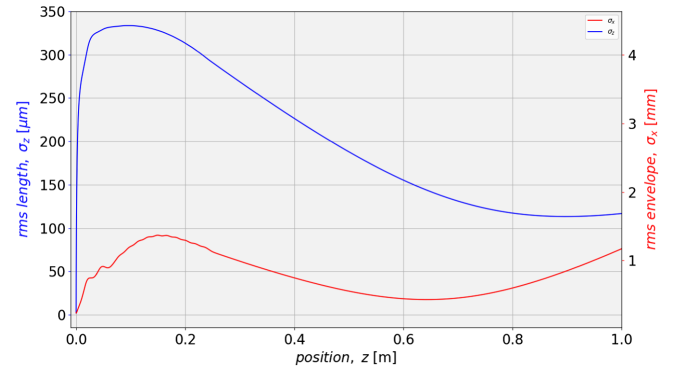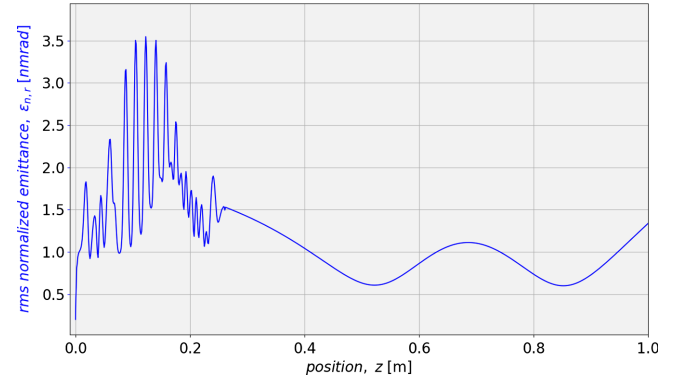

(b) Normalized rms emittance

FIG. 11.   Behavior of the rms parameters (a) and the rms normalized emittance (b) up to 1 m downstream the cathode.

IV. BEAM DYNAMICS IN THE DRIFT

In the simulations, a lengthy drift was added after the hybrid photoinjector exit to allow the beam to evolve toward optimization of its physical properties through compression and emittance compensation.

We show in Fig. 11 the behavior of the rms parameters (a) and the rms normalized emittance (b) up to a position of 1 m from the cathode.

A. Slice analysis

In order to perform a more detailed analysis of beam dynamics, we analyzed the behavior of the beam slice. To do this, we have utilized the data obtained from simulation code GPT that produced the results discussed above. We binned the bunch distribution into ten longitudinal slices at the photocathode (Fig. 12). Each slice has the same initial longitudinal size and so they are populated by a different number of particles, as to the injected particle distribution is not longitudinally uniform. Particles of each slice are marked with different colors, which they maintain throughout the analysis along the entire beamline.

This type of analysis allows us to observe the bunch evolution [Fig. 12(a)] to examine the possible mixing of slices and, more importantly, the transverse [Fig. 12(b)] and longitudinal [Fig. 12(c)] slice phase spaces.

FIG. 10.   Normalized transverse emittance for two-beam transverse distributions: Gaussian (red) and uniform (blue).
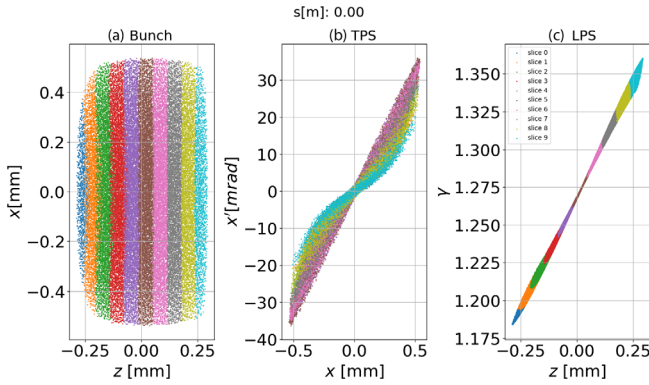
FIG. 12.   (a) Slice partition at the cathode, (b) slice transverse phase space, and (c) energy-position correlation.

A small artifact is noted in implementing the slice analysis: the binning into longitudinal slices is performed at a distance $z = 0.001$ m from the cathode. This is done so that all macroparticles in the simulation are emitted by this point. For this reason in Fig. 12(b), we observe that in the transverse phase space there is already a correlation between x and x'. This correlation does not produce, necessarily, emittance growth, as it is obtained by examining an instant in time t, as opposed to a single value of z as one should rigorously use to describe the emittance. The rounded shape at the tail of the beam observed in Fig. 12(a) is due to the effects of the image charges at the cathode.

The effects of a range of relevant beam processes, such as velocity bunching, space-charge effects [49,50], and compression are revealed by this analysis. Such effects are prominently apparent in Fig. 13 which shows the beam reaching an ellipsoidal shape near the emittance minimum position ($z = 0.52$ m) and the modified transverse and longitudinal phase spaces. We note that a significant correlation of the longitudinal phase space persists (longitudinal laminarity) during the bunch longitudinal minimum (waist), which is the evidence of a space-charge-dominated behavior. This type of analysis also reveals insight into the
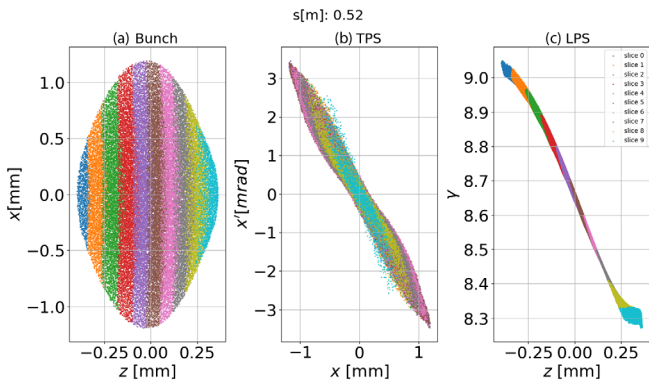

FIG. 13.   Modified bunch (a) shape and (b) transverse and (c) longitudinal phase space properties at the emittance minimum ($z = 0.52$ m).
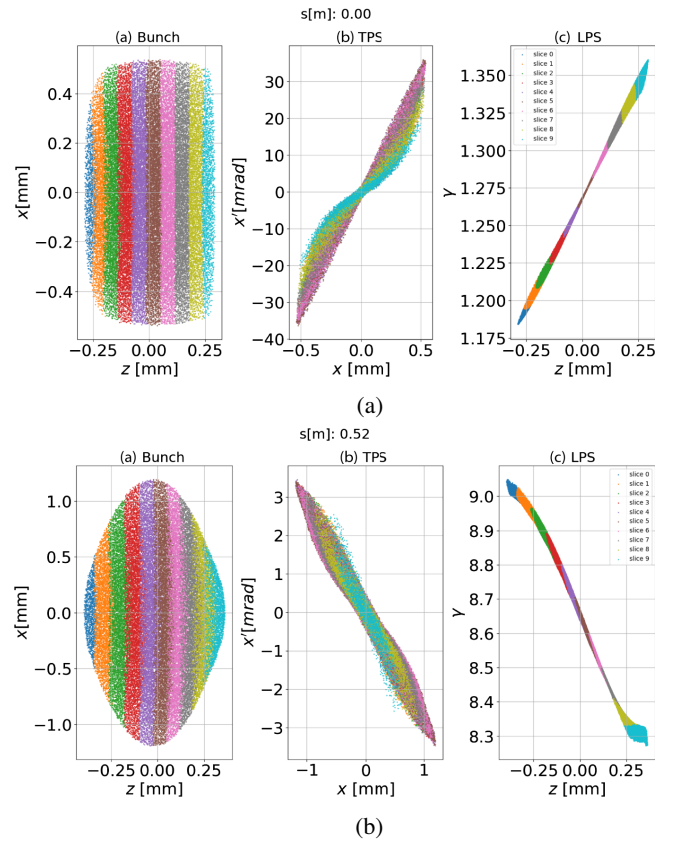

FIG. 14.   Slices analysis for uniform distribution. (a) Slices partition at the cathode position ($z = 0$ m) (b) Slices partition at the emittance minimum ($z = 0.52$ m).

reasons why the truncated Gaussian distribution produces a reduction in the output emittance.

In the flattop case, we observe in the plots shown in (Fig. 14) that the shape of the slices in the transverse phase space is not linear, while for the truncated Gaussian case they are much closer to this ideal linear form. This is evidenced by the shape of the beam generated [Fig 14(a)], but it is also reflected in the improvement of the emittance minimum [Fig 14(b)]. The reason for this behavior lies in the fact that a truncated Gaussian distribution is similar to the ideal parabolic distribution that produces longitudinal blowout. As a result, the space-charge forces inside the beam become nearly linear almost immediately [51] upon emission. This longitudinal blowout [52–54] is reinforced by the subsequent transverse blowout, which is also initiated efficiently by a distribution close to the final ellipsoidal form desired.

B. Ellipsoidal shape

The evolution of the beam slices investigated so far suggests that, as the bunch leaves the hybrid photoinjector, it forms and maintains a nearly ellipsoidal shape during expansion and compression. This statement may be quantified in two complementary ways. In the first approach, a geometric analysis was carried out with the distribution
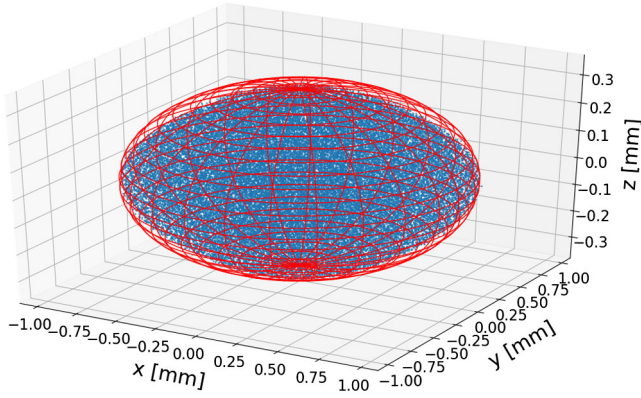
FIG. 15. Demonstration of the ellipsoidal shape. The red grid is the shape of the ellipsoid surface of Eq. (2) with semiaxes $a = b = \sigma_x \sqrt{5}$ and $c = \gamma \sigma_z \sqrt{5}$ and $u = 1$ evaluated at the waist position $z = 0.64$. The blue dots are the 3D distribution particles at the waist position, too.

compared to a parametric ellipsoid described by the following equation:

$$\mathcal{E}'(u): \frac{x^2}{a^2 u^2} + \frac{y^2}{b^2 u^2} + \frac{z'^2}{c^2 u^2} = 1, \quad (2)$$

where $u \in (0, 1]$ and a, b, and c are the principal semiaxes of the ellipsoid in the beam frame—notice, in fact, that quantities exhibit the "prime" symbol. As can be seen in Fig. 15, the beam is contained within the ellipsoidal boundary with the semiaxes values obtained from the rms parameter of the bunch ($a = b = \sigma_x \sqrt{5}$ and $c = \gamma \sigma_z \sqrt{5}$) and $u = 1$.

In Fig. 16, the complementary expectation for the uniformly filled ellipsoid is validated, as we show the uniformity of the resultant beam density after ellipsoidal boundaries are reached. This binned plot shows remarkably constant uniformity in the density distribution, with small statistical artifacts present. There is also a region near the ellipse boundary with irregular density, an effect arising
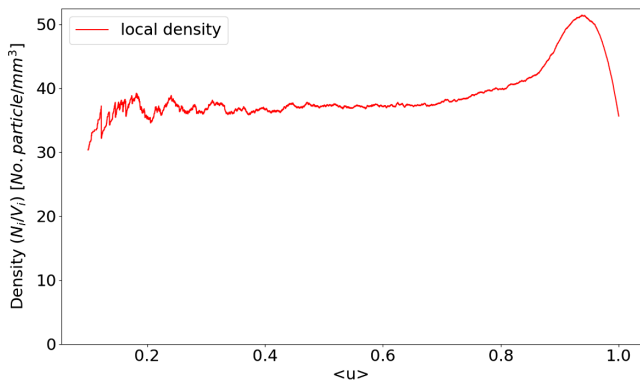

FIG. 16. Spatial binning of beam density, showing the development of a uniform distribution.

from nonlinear fields and accompanying effects such as wave breaking [55].

C. Ellipsoidal space-charge forces

The achievement of a nearly ellipsoidal distribution greatly simplifies the analysis of the beam dynamics during acceleration, where we must confront the simultaneous need to understand very powerful rf focusing, space-charge, and wakefield effects. The ellipsoidal beam, as described above, permits an elegant implementation of the space-charge effects through a straightforward, accurate analytical model. Following the long-established methods introduced in [51], we consider a charge Q homogeneously filling the ellipsoidal volume inside the boundary described by

$$\mathcal{E}': \frac{x^2}{a^2} + \frac{y^2}{b^2} + \frac{z'^2}{c^2} = 1, \quad (3)$$

where a, b, and c are, as above, the principal semiaxes of the ellipsoid. In the reference frame comoving with the beam, where the electrons are nearly at rest, the electrostatic potential for a point inside the ellipsoidal surface is given by

$$
\begin{aligned}
\Phi'(x, y, z') = \frac{3Q}{16\pi\epsilon_0} \int_0^{+\infty} &\left(1 - \frac{x^2}{a^2 + t}\right. \\
&\left. + - \frac{y^2}{b^2 + t} - \frac{z'^2}{c^2 + t}\right) \frac{dt}{\sqrt{\varphi(t)}} \\
\equiv D_0 &- A_0 x^2 - B_0 y^2 - C_0 z'^2, \quad (4)
\end{aligned}
$$

where $\varphi(t) = (a^2 + t)(b^2 + t)(c^2 + t)$ is an auxiliary function and the coefficients from A_0 to D_0 depend only on the semiaxes ratios a/b, a/c and on the total charge (see also [56]). Inside the distribution, the field derived from the quadratic potential in (4) grows linearly with the displacement from the center in all three directions yielding linear forces in the beam reference frame [53,54].

Field linearity along the axes is preserved by Lorentz transformations and, therefore, it still holds in the laboratory frame where the relevant changes in momentum are calculated. Such behavior results in a very special regime: A uniform ellipsoid subjected to linear forces, both self-induced (e.g., space charge) and applied externally (solenoid, quadrupole), can expand and contract changing its size and orientation but it maintains the uniform ellipsoidal shape in the limit of space-charge-dominated behavior. As a consequence, in this regime, the space-charge forces derived from (4) provide a self-consistent model for the evolution of the beam, without the need to consider of emittance-induced dynamics.

In order to investigate this special behavior, we compare the evolution of the actual beam produced by the hybrid gun with the case of ellipsoidal self-induced forces. To do
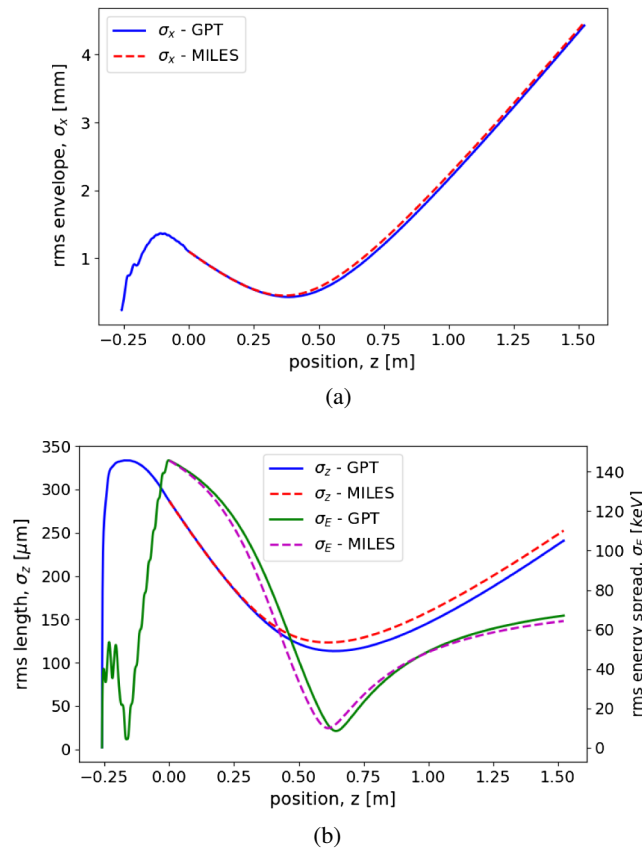
(a)

(b)

FIG. 17.   Second order moments (rms length σ_z and rms energy spread σ_E) of the beam distribution in a ~1.5 m long drift space. Comparison between GPT (solid lines, blue for σ_z, and green for σ_E) and custom tracking with ellipsoidal space-charge forces (dashed lines, red for σ_z, and purple for σ_E). The tracking starts at $z = 0$ where the beam exits the hybrid photoinjector. (a) Transverse plane. (b) Longitudinal plane.

so, we exploit MILES: a custom tracking code developed by us for studying the effects of transverse wakes in linacs [57]. In particular, such code uses the analytical model for a uniformly charged ellipsoid described above to account for both transverse and longitudinal space charge forces.

In Fig. 17, we show the evolution of the electron beam parameters obtained from the hybrid photoinjector in the drift space of length ~1.5 m. The plot shows the rms transverse envelope, the rms bunch length, and the rms energy spread evaluated with the tracking code MILES (dashed lines) in comparison with the original results from GPT (solid lines). For simplicity, we chose $z = 0$ to be located at the exit of the TW section where the drift region starts. As the beam propagates in absence of external fields, it is only subjected to self-induced forces. Therefore, the agreement shown in this comparison illustrates that the assumption of a quasi-uniform ellipsoidal shape for calculating the collective space-charge forces is quite satisfactory.
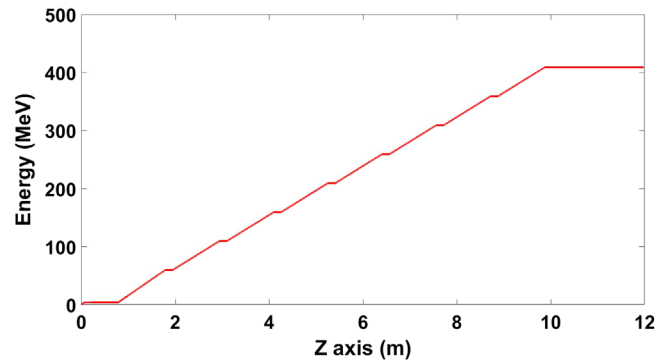

FIG. 18.   The beam energy gain from the cathode at $z = 0$ m up to the end of the beamline with eight high-gradient linacs.

V. EXTENSION TO HIGH ENERGY OPERATION

In this section, we investigate the extension of the injector operation to reach high electron energy. In particular, the following topics have been addressed: (a) Acceleration and beam dynamics management to 400 MeV in eight Tantawi-style [58] structures; (b) beam breakup, short-range wakefields as well as alignment tolerances in advanced light sources.

A. Beam dynamics in the high energy scenario

Eight linac sections based on a distributed coupling geometry developed by Tantawi *et al.* [58], operated at 50 MV/m accelerating gradient, are used. The first linac is located at ~80 cm from the hybrid photoinjector. The beam energy gain up to ~400 MeV is given in Fig. 18. It can be noted that the first linac gradient is slightly higher than the other ones in order to obtain close matching of beam envelope to the invariant envelope [37].

As discussed above, full 6D phase space compensation was obtained just upstream to injection into the linacs. All parameters were optimized in order to obtain beam emittance minimization, to $\epsilon_n = 0.5$ mm mrad, as shown in Fig. 19. This condition is reached simultaneously with bunch compression down to $\sigma_z = 200$ fs (see Fig. 20),
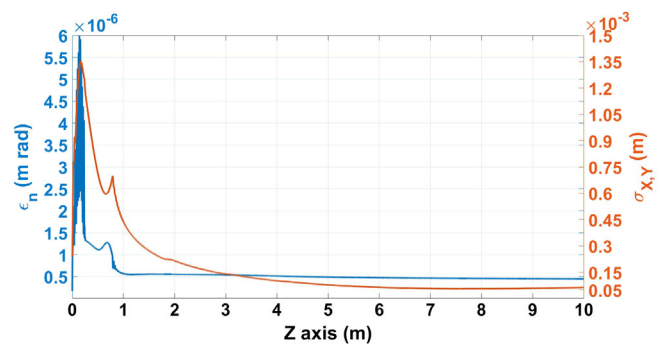

FIG. 19.   Evolution of the rms transverse beam size $\sigma_{x,y}$ and normalized transverse emittance ϵ_n along the beamline; beam charge 250 pC, energy 400 MeV.
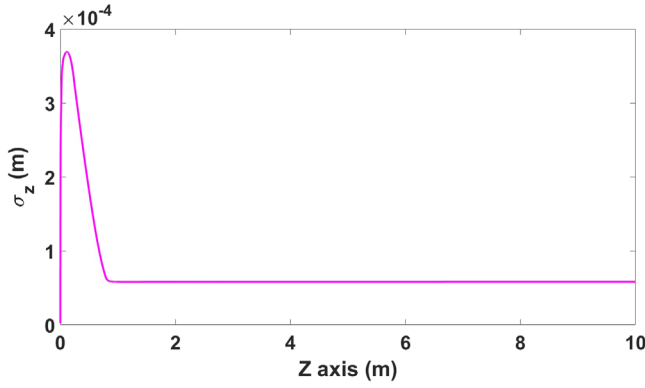
FIG. 20. Evolution of the rms bunch length σ_z along the beamline; beam charge 250 pC, energy 400 MeV.
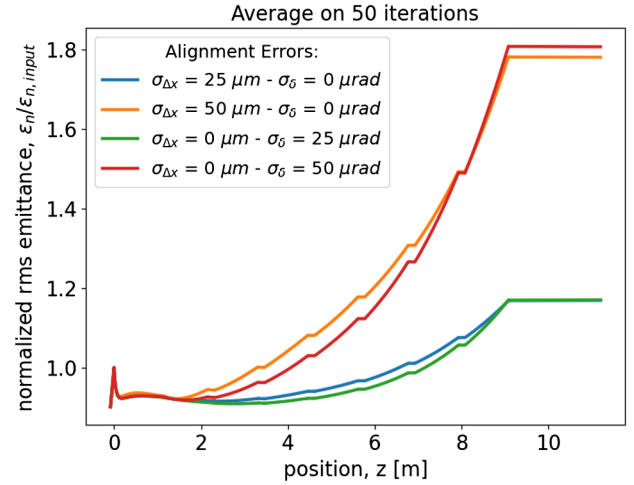

FIG. 21. rms emittance dilution induced by random alignment errors in a eight-section linac. The input location is $z = 0$ and the emittance is normalized by its injection value.

corresponding to a beam peak current above 600 A. These parameters, as discussed further below, are attractive for advanced applications.

B. Beam breakup, alignment tolerances, and trajectory corrections

Linac sections exploiting distributed coupling techniques have the advantages of enhancing the accelerating gradient as well as the transverse focusing due to rich content in nonsynchronous space harmonics [45,50]. Nevertheless, small cell irises are also accompanied by strong wakefield interactions which may threaten the nominal beam quality [38]. In linacs, the major effect of this kind arises from the transverse dipole component of the electromagnetic field excited by particles traveling off axis in the structure. The strength of the corresponding interaction in periodic accelerating cavities is described by Bane's wake function and scales approximately as the inverse third power of the iris radius [59].

The excitation of dipole wakefields due to particles traveling off axis can be considerably enhanced when machines are subjected to alignment errors which will cause deviations from the nominal trajectory. Such imperfections can lead to a significant phase space dilution and, therefore, it is crucial to investigate alignment tolerances in order to ensure the design performance.

In the following, we present a study on random alignment errors affecting the eight-section linac used to arrive at the energies needed for the application of this injector to the light sources. The simulations are performed with MILES [57], the tracking code introduced previously which employs the space-charge forces in ellipsoidal distributions. This computational tool also accounts for the short-range transverse wakefields by means of the so-called *wakefield matrix* formalism [60,61], which permits straightforward inclusion of rf acceleration as well as transverse forces.

The code thus provides a unique model for examining BBU, including effects—rf focusing and strong space

charge—that extend beyond the usual high energy approximations.

For simplicity, our current analysis investigates separately the effects of random transverse offsets and tilt angles with respect to the main linac axis although the two effects can be easily combined. The analysis assumes alignment errors (offsets Δx_i or tilt angles $\delta_i, 1 \leq i \leq 8$) with a Gaussian distribution for which the standard deviation ($\sigma_{\Delta x}$ or σ_δ) can be chosen arbitrarily. A large number (e.g., 50) of simulations are performed changing in each instance the set of random errors. The rms emittances obtained are then averaged in order to mitigate the statistical fluctuations. In Fig. 21, the emittance, normalized to its value at injection, is shown for different values of the characteristic errors.

The picture suggests that for alignment errors below 25 microns the emittance growth is limited and should not notably degrade the beam quality. In addition, this tolerance is a feasible value, achievable through suitable surveying procedures (see, e.g., [62]). It has to be noticed that the mechanical alignment which can be achieved with C-band structures is below 50 μm [63,64], thus reassuring that our error tolerance analysis leads to a constraint which is then feasible. Conversely, the emittance dilution is not negligible for errors of increasing entity, as shown for the 50 microns case, and correction schemes based on steering magnets should be considered. In order to demonstrate the efficacy of beam-based alignment (BBA) methods, we apply the so-called *one-to-one* steering algorithm [65] for the following reference case.

Let us assume that the first accelerating section of the linac is shifted in the transverse plane with an offset $\Delta x_1 = 50\ \mu$m. In order to compensate for the deviations from the nominal trajectory, we also assume a set of beam position monitors (BPMs) and steering dipole magnets.

The former measures the transverse displacement of the beam center of mass whereas the latter applies correction kicks in the transverse plane according to the Lorentz force acting on a charge q with rest-mass m_e

$$\Delta x' = \int \frac{F_x}{\beta^2 \gamma m_e c^2} dz = -\frac{qK}{\beta \gamma m_e c} \qquad (5a)$$

$$K = \int B_y(z) dz, \qquad (5b)$$

where K is the integrated dipole field and accounts for the corrector strength. The resulting lattice foresees a dipole kicker upstream and a BPM reader downstream for each linac module so that the corrections can be adjusted as a function of the BPM measurements. Indeed, one-to-one algorithms aim to find the field strength in the steering magnets which ensures zero transverse offset at BPM's locations.

The application of the algorithm is shown in Fig. 22 for the reference case described above. For comparison, additionally, the results for an ideal machine with no misaligned sections are shown by the green squares. We note that without corrections (red triangles), the beam travels away from the nominal axis and excites dipole wakefields, thus increasing the emittance by a factor ∼2. Conversely, if the corrections provided by the one-to-one algorithm are applied, the new trajectory (black dashed curves) intersects the nominal axis at the BPM locations indicated by the gold crosses. However even though the corresponding emittance growth reduces significantly, it is not avoided entirely, since the algorithm aims for a local optimization of the trajectory rather than a global emittance minimization. Alternative approaches based on the "dispersion-free steering" strategy [66] will be investigated in future work in order to achieve a global correction yielding the minimum rms emittance.

VI. APPLICATIONS

With both the performance of the injector and postacceleration systems well-optimized, we can proceed to discuss applications enabled by the unique characteristics of this compact, high-brightness electron beam source. We have investigated two possible scenarios: application to inverse Compton scattering and free electron laser (FEL) sources. Both of these employ, by necessity, moderately high energies (in the 300–500 MeV range) to reach the relevant photon characteristics. There are also other possible applications that are not critically dependent on the electron beam energy (e.g., creation of narrow-band THz radiation through driving dielectric wakefield structures [67]).

A. Inverse Compton scattering source

In order to meet the requirements of the final focusing for low bandwidth and very high flux inverse Compton scattering (ICS) source, we have studied the final focusing
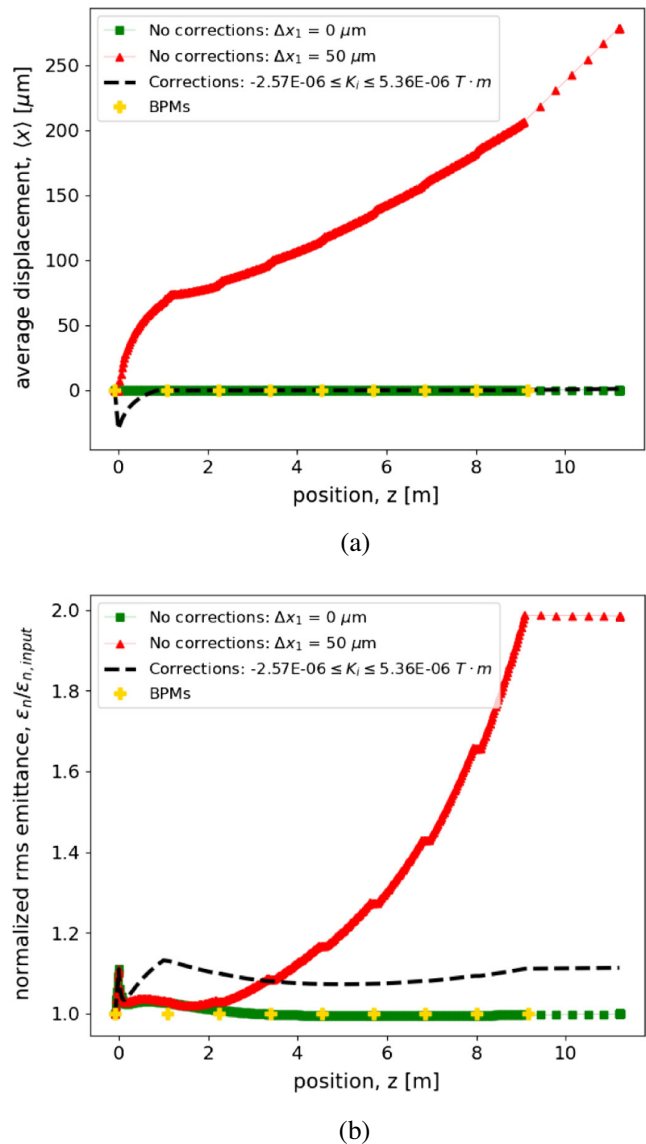

(a)

(b)

FIG. 22. Demonstration of one-to-one steering algorithms. Green squares represent an ideal machine with no misalignments while red triangles represent a linac whose first section is 50 μm off axis. Introducing the magnetic corrections according to one-to-one procedures, the new trajectory and emittance are given by the black dashed curves. The gold crosses identify the location of the BPMs. (a) Center of mass trajectory. (b) Normalized rms emittance growth.

scheme for a beam, in an intermediate medium-energy case at 220 MeV, obtained using four linac sections). The focal system is composed of a tunable permanent magnet triplet array [68,69] with lengths of 6 cm-12 cm-6 cm and nominal gradients of 102 T/m-94 T/m-102 T/m, respectively.

Start-to-end simulations of this scenario have been performed with the GPT code. The full beam envelope evolution is shown in Fig. 23 while Fig. 24 shows the interaction region which illustrates the predicted very compact (below 9 μm) spot sizes.
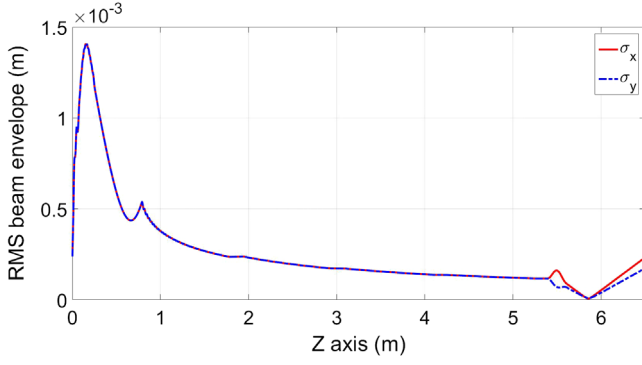
FIG. 23. rms beam sizes σ_x and σ_y in ICS system operated at 220 MeV, from GPT start-to end simulation.
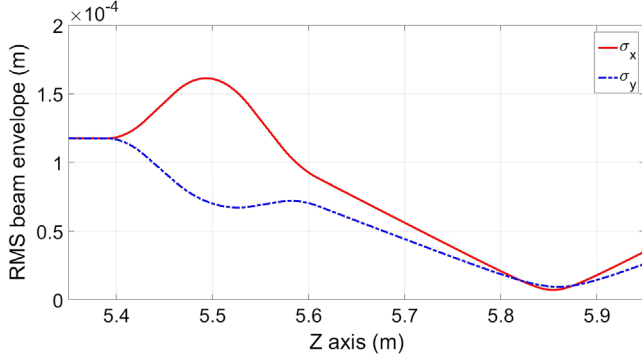

FIG. 24. rms beam sizes σ_x and σ_y in final focus system at 220 MeV from GPT start-to end simulation.

Indeed, a variation on the hybrid photoinjector presented here is now being used to realize a high flux, narrow band (high brilliance) ICS sources of gamma rays, in a project including the present authors and led by RadiaBeam Technologies. To give an idea of the capabilities of the currently discussed system for such an application, we assume a collision of the (frequency-doubled Ti:Sapphire) laser beam with a 0.4 μm wavelength laser focused to the same spot, or $w_0 \simeq 14$ μm, containing total pulse energy of $U_l = 200$ mJ. In this case, we can write the total number of Compton photons produced per collision as

$$N_\gamma = \frac{N_e U_l}{4\pi\hbar\omega_l\sigma_x\sigma_y}\sigma_T, \tag{6}$$

where $\sigma_T = 2\alpha^2\lambda_c^2/3\pi \simeq 6.65 \times 10^{29}$ m^2 is the Thomson cross section. For the parameters given, the flux per collision of gamma rays, having nominal peak energy per photon $u_\gamma \simeq 2.3$ MeV, is $N_\gamma \simeq 3.5 \times 10^7$ photons. This estimate includes all scattered photon energies.

For applications that are sensitive to the spread of photon energy, there are numerous contributions to the final relative bandwidth of the ICS pulse to take into account [70–72]. This is an exercise beyond the present article's scope, but there are a few dominant effects that should be

mentioned in the context of the hybrid injector as presented. In order to achieve low final bandwidth, one should remove the inhomogeneous broadening through off-axis red-shifting by collimation, which leaves a few percent of the photons surviving. The bandwidth is then limited by homogeneous processes, notably due to the angles in the beam electrons and the nonlinear redshifting, In the first case, the relative bandwidth is $\mathrm{BW}_\theta \simeq \sigma'_x\gamma/\sqrt{2} = \epsilon_n/\sqrt{2}\sigma_x \simeq 5.5 \times 10^{-3}$.

Likewise, the nonlinear interaction component is estimated to be $\mathrm{BW}_{NL} \simeq a_L^2/2$ [73]. Here a_L is the normalized vector potential associated with the laser and is obtained by evaluating the laser intensity through $a_L^2 = 7.3 \times 10^{-19}\lambda(\mu m)$, with the intensity $I = U_l c/\sqrt{2\pi}\sigma_l w_0^2$ quoted in W/cm^2. The final focus gives an upper limit on the laser pulse length, as to avoid the "hour-glass" effect of diminishing the luminosity [71], one cannot choose the laser pulse length $\sigma_l \leq Z_R$, and so the intensity of the laser is given, as $I \geq U_l c/\sqrt{2\pi}w_0^3$. For our example, we have a $I \geq 8.5 \times 10^{17}$ W/cm^2. The contribution to the relative bandwidth from nonlinear effects is thus estimated as $\mathrm{BW}_{NL} \simeq 4.6 \times 10^{-2}$.

Finally, we note that in photoinjector-driven ICS sources, there is an important effect that arises from misalignment or jitter in the transverse position of the laser impinging on the photocathode. Small deviations from alignment can be relatively magnified at the final focus, as while the envelope is focused at a strength partly specified by space-charge effects, this outward force is not present in setting the trajectory of the beam centroid. Thus there is a mismatch in the beam centroid optics and those of the envelope; an offset at the photocathode is not minimized at the IP in general. We illustrate this effect in Fig. 25. It can be seen that the initial misalignment of 100 microns at the photocathode leaves a residual misalignment at the IP of 11 microns. Comparing this to the beam sizes at the IP, we should require that the misalignment (systematic or jitter-induced) at the photocathode be no larger than
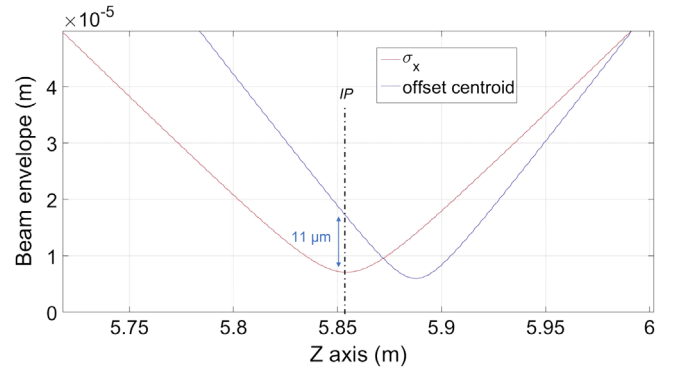

FIG. 25. Beam centroid offset and beam envelope near the Compton interaction point, with an initial misalignment of the centroid of laser on the photocathode of 100 microns.
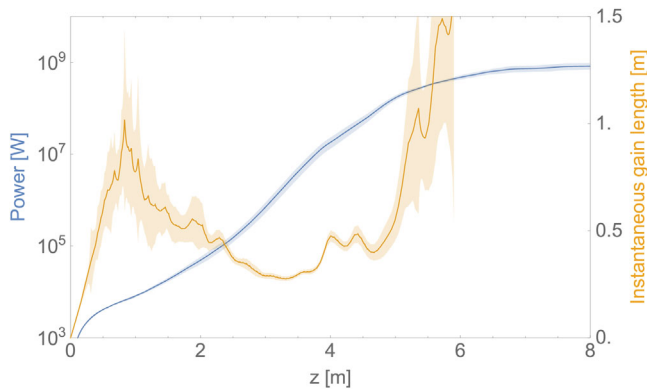
FIG. 26.   Instantaneous gain length (orange) and laser power (blue) as calculated in GENESIS. The peak power at saturation is approximately 830 MW.
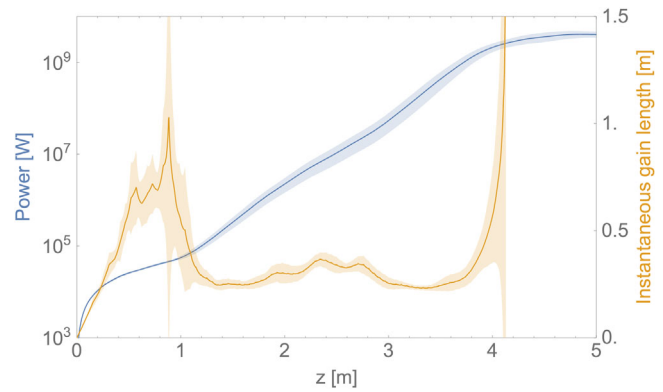

FIG. 27.   Instantaneous gain length (orange) and laser power (blue) as calculated in GENESIS for water window (4 nm) soft x-ray FEL. The peak power at saturation is approximately 4.2 GW.

25 microns. This is similar to the requirement arising from consideration of short-range BBU in isolation; the misalignment indeed seeds the BBU effects described above.

The optimization of parameters to achieve the desired source property such as peak spectral brilliance is apparent from this brief discussion. We also note, in regards to the final focus example given here, that the beam optics system described above is straightforwardly scalable to lower beam energies (around 100 MeV), in which case the use of standard normal conducting electromagnets with gradients around 20 T/m is permitted.

B. Short wavelength free-electron laser

Simulations modeling the original design of the hybrid photoinjector in high energy operation have suggested it to be suitable for use as an x-ray FEL injector. In this application, the gain length and photon-per-pulse output profit from the considerable longitudinal compression the hybrid design imparts, and the consequently high peak current. Linear transformations matching the transverse phase-space orientation were performed to optimize the gain through an 8 m FD lattice with 15 T/m quadrupoles in GENESIS [74]. These optimal matching dimensions, along with other relevant simulation parameters, are reported below in Table III.

The GENESIS simulation results, as shown in Fig. 26, indicate saturation and lasing at $\lambda = 6.0$ nm, with a mean single shot energy output of 62 μJ. It should be noted that

TABLE III.   FEL simulation input parameters.

Parameter	Value
Beam charge, Q	250 pC
Spot dimensions, $\sigma_{x,y}$	22×15 μm
Normalized emittance, $\epsilon_{n,r}$	0.50 mm mrad
Bunch length, σ_z	190 fs
Mean energy, γmc^2	400 MeV
Fractional energy spread	0.054%

the transverse tuning required to match the beam to the FD lattice can be obtained with quadrupoles and solenoids alone. In particular, no bunch compression mechanism is required, with the hybrid design's ability to effect simultaneous 6D phase space compensation relieving us of the difficulties (e.g beam self-interaction through CSR and transverse emittance growth) associated with postacceleration compression.

With a slight expansion of the system footprint, by adding two more linac sections (thus increasing to the final energy and permitting off-crest operation in part of the linac) as well as a compact ($\sim$1 m) chicane, we can enable a soft x-ray FEL operating in the water window at $\lambda = 4$ nm. The performance of this system is summarized in Fig. 27. The increased current has a dramatic effect on the peak power (4.2 GW is predicted), by introducing higher peak electron beam power and by increasing ρ by 50%. The resulting Pierce parameter is $\rho = 1.4 \times 10^{-3}$. This is consistent with the expected extraction fraction of electron beam peak power.

VII. CONCLUSIONS

We have presented the rf and beam dynamics optimization analysis of a new class of a compact hybrid (SW/TW) photoinjector for next generation linac accelerator-based research facilities. To illustrate the use of this type of optimized injector, several examples of high performance applications are discussed. While we restrict the discussion here to the two examples of ICS and FEL sources, many other state-of-the-art capabilities (e.g., wakefield accelerators, THz sources) are introduced by this compact device.

The photoinjector studied in detail operates in C-band at 5.712 GHz, where the rf model has been optimized to operate with an electric field of 120 MV/m at the cathode, which is at the present state-of-the-art for normal temperature gun structures. This optimization has permitted a modest input power requirement of <20 MW.

The beam dynamics analysis has been carried out with the purpose of obtaining a full 6D emittance compensation (both on the transverse and longitudinal planes) with a 250 pC electron bunch. The simultaneous focus out to the hybrid, achieved immediately upstream of the postacceleration linac, produces a uniformly filled ellipsoidal beam distribution that indeed approaches spherical shape. This gives a unique system in which to study single component plasma physics dynamics; such a study is now underway. This optimization has also produced very high beam quality in simulation, as it yielded excellent emittance compensation along with strong compression to give high peak current—a very high 5D beam brightness is achieved. In the course of the optimization study, we have found a remarkably strong dependence on the beam's transverse distribution launched at the cathode. By choosing a truncated Gaussian as opposed to a uniform distribution, we diminish the normalized transverse emittance from 0.7 to 0.5 mm mrad. This result is quite interesting, as it is at odds with some traditional notions concerning mitigation of space-charge forces. The observation that the beam is a nearly uniformly filled ellipsoid after the gun also permits the development of powerful new tools for including space-charge forces in beam-breakup simulations. These tools will be described in a forthcoming work.

With such attractive beam properties, we have investigated the application of the compact C-band hybrid photoinjector to a number of advanced scenarios. First, we have examined as the injector of an intermediate energy (220 MeV) ICS monochromatic gamma-ray source, which takes advantage of the beam focusability and its short pulse length. Indeed, we have studied a working point which utilizes a beam spot size less than 10 μm at the interaction point located at less than 6 m from the cathode. The compactness of this system is attractive in applications requiring a mobile source. We then proceed to investigate a higher energy (400 MeV) soft x-ray FEL. Again with a modest footprint, we demonstrated the possibility of lasing at 4 nm, producing a compact water-window free-electron laser in 10 m length. For completeness, we note that the utility of the hybrid injector in application is validated by studies of beam stability and alignment tolerances, issues which are more challenging in this very high performance system.

Looking to the future, we intend to scale this hybrid structure design further, to higher rf frequency and higher accelerating gradients. This will entail the use of cryogenic cooling to avoid breakdown issues and mitigate power requirements.

[1] V. Shiltsev and F. Zimmermann, Modern and future colliders, Rev. Mod. Phys. **93**, 015006 (2021).

[2] L. Schoeffel, C. Baldenegro, H. Hamdaoui, S. Hassani, C. Royon, and M. Saimpert, Photon–photon physics at the LHC and laser beam experiments, present and future, Prog. Part. Nucl. Phys. **120**, 103889 (2021).

[3] J. Rosenzweig, N. Majernik, R. Robles, G. Andonian, O. Camacho, A. Fukasawa, A. Kogar, G. Lawler, J. Miao, P. Musumeci *et al.*, An ultra-compact x-ray free-electronlaser, New J. Phys. **22**, 093067 (2020).

[4] L. Faillace, R. Agostino, A. Bacci, R. Barberi, A. Bosotti, F. Broggi, P. Cardarelli, S. Cialdi, I. Drebot, V. Formoso *et al.*, Status of compact inverse Compton sources in Italy: BriXS and STAR, in *Proceedings of SPIE 11110, Advances in Laboratory-based X-Ray Sources, Optics, and Applications VII* (2019), p. 1111005, 10.1117/12.2531168.

[5] L. Rigon, 2.08—x-ray imaging with coherent sources, in *Comprehensive Biomedical Physics*, edited by A. Brahme (Elsevier, Oxford, 2014), pp. 193–220.

[6] W. Graves, High brilliance x-rays from CompactSources, in *Proceedings of the High Brightness Electron Beams Workshop, San Juan, PR, 2013*, http://pbpl.physics.ucla.edu/HBEB2013/Talks/WilliamGravesHBEB13.pptx.

[7] B. Carlsten, New photoelectric injector design for the Losalamos National Laboratory XUV FEL Accelerator, Nucl. Instrum. Methods Phys. Res., Sect. A **285**, 313 (1989).

[8] F. Zhou, C. Adolphsen, A. Benwell, G. Brown, D. H. Dowell, M. Dunning, S. Gilevich, K. Grouev, G. Huang, B. Jacobson, X. H. Liu, A. Miahnahri, F. Sannibale, J. Schmerge, and T. Vecchione, Commissioning of the SLAC linac coherent light source II electron source, Phys. Rev. Accel. Beams **24**, 073401 (2021).

[9] R. R. Robles, O. Camacho, A. Fukasawa, N. Majernik, and J. B. Rosenzweig, Versatile, high brightness, cryogenic photoinjector electron source, Phys. Rev. Accel. Beams **24**, 063401 (2021).

[10] R. Nagai, R. Hajima, N. Nishimori, T. Muto, M. Yamamoto, Y. Honda, T. Miyajima, H. Iijima, M. Kuriki, M. Kuwahara, and S. Okumi, High-voltage testing of a 500-kV dc photocathode electron gun, Rev. Sci. Instrum. **81**, 033304 (2010).

[11] P. A. Adderley, J. Clark, J. Grames, J. Hansknecht, K. Surles-Law, D. Machie, M. Poelker, M. L. Stutzman, and R. Suleiman, Load-locked dc high voltage GaAs photogun with an inverted-geometry ceramic insulator, Phys. Rev. ST Accel. Beams **13**, 010101 (2010).

[12] C. Gulliford, A. Bartnik, I. Bazarov, B. Dunham, and L. Cultrera, Demonstration of cathode emittance dominated high bunch charge beams in a dc gun-based photoinjector, Appl. Phys. Lett. **106**, 094101 (2015).

[13] B. M. Dunham, C. K. Sinclair, I. V. Bazarov, Y. Li, X. Liu, and K. W. Smolenski, Performance of a very high voltage photoemission electron gun for a high brightness, high average current ERL injector, in *Proceedings of the 22nd Particle Accelerator Conference, PAC-2007, Albuquerque, NM* (IEEE, New York, 2007), pp. 1224–1226.

[14] T. Asaka, H. Ego, H. Hanaki, T. Hara, T. Hasegawa, T. Hasegawa, T. Inagaki, T. Kobayashi, C. Kondo, H. Maesaka, S. Matsubara *et al.*, Low-emittance thermionic-gun-based

injector for a compact free-electron laser, Phys. Rev. Accel. Beams **20**, 080702 (2017).

[15] J. Teichert, A. Arnold, G. Ciovati, J. C. Deinert, P. Evtushenko, M. Justus, J. M. Klopf, P. Kneisel, S. Kovalev, M. Kuntzsch, and U. Lehnert, Successful user operation of a superconducting radio-frequency photoelectron gun with Mg cathodes, Phys. Rev. Accel. Beams **24**, 033401 (2021).

[16] A. Arnold and J. Teichert, Overview on superconducting photoinjectors, Phys. Rev. ST Accel. Beams **14**, 024801 (2011).

[17] I. Pinayev, V. N. Litvinenko, J. Tuozzolo, J. C. Brutus, S. Belomestnykh, C. Boulware, C. Folz, D. Gassner, T. Grimm, Y. Hao, and J. Jamilkowski, High-gradient high-charge CW superconducting rf gun with CsK2Sb photocathode, arXiv:1511.05595.

[18] M. Ferrario, D. Alesini, A. Bacci, M. Bellaveglia, R. Boni, M. Boscolo, M. Castellano, L. Catani, E. Chiadroni, S. Cialdi, and A. Cianchi, Direct Measurement of the Double Emittance Minimum in the Beam Dynamics of the Sparc High-Brightness Photoinjector, Phys. Rev. Lett. **99**, 234801 (2007).

[19] D. H. Dowell, E. Jongewaard, C. Limborg-Deprey, J. Schmerge, Z. Li, L. Xiao, J. Wang, J. Lewandowski, and A. Vlieks, Results of the SLAC LCLS gun high-power rf tests, in *Proceedings of the 22nd Particle Accelerator Conference, PAC-2007, Albuquerque, NM* (IEEE, New York, 2007), pp. 1296–1298.

[20] G. Penco, E. Allaria, L. Badano, P. Cinquegrana, P. Craievich, M. Danailov, A. Demidovich, R. Ivanov, A. Lutman, L. Rumiz, and P. Sigalotti, Optimization of a high brightness photoinjector for a seeded FEL facility, J. Instrum. **8**, P05015 (2013).

[21] L. Faillace, R. Agustsson, P. Frigola, and A. Verma, Status of the FERMI II RF Gun at Sincrotrone Trieste, in *Proceedings of the 27th International Linear Accelerator Conference, LINAC-2014, Geneva, Switzerland* (JACOW Publishing, Geneva, Switzerland, 2014), pp. 692–694.

[22] J. Hong, J. H. Han, and C. K. Min, Performance of S-band photocathode rf gun with coaxial coupler, in *Proceedings of the 39th Free Electron Laser Conference (FEL'19), Hamburg, Germany, 2019* (JACOW Publishing, Geneva, Switzerland), pp. 481–483.

[23] J. B. Rosenzweig, A. Cahill, V. Dolgashev, C. Emma, A. Fukasawa, R. Li, C. Limborg, J. Maxson, P. Musumeci, A. Nause, and R. Pakter, Next generation high brightness electron beams from ultrahigh field cryogenic rf photocathode sources, Phys. Rev. Accel. Beams **22**, 023403 (2019).

[24] A. D. Cahill, J. B. Rosenzweig, V. A. Dolgashev, S. G. Tantawi, and S. Weathersby, High gradient experiments with X-band cryogenic copper accelerating cavities, Phys. Rev. Accel. Beams **21**, 102002 (2018).

[25] T. Luo, H. Feng, D. Filippetto, M. Johnson, A. Lambert, D. Li, C. Mitchell, F. Sannibale, J. Staples, S. Virostek, and R. Wells, rf design of APEX2 two-cell continuous-wave normal conducting photoelectron gun cavity based on multi-objective genetic algorithm, Nucl. Instrum. Methods Phys. Res., Sect. A **940**, 12 (2019).

[26] G. Shu, Y. Chen, S. Lal, H. J. Qian, H. Shaker, and F. Stephan, First design studies of a NC CW rf gun for European XFEL, in *Proceedings of the 10th International Particle Accelerator Conference, IPAC-2019, Melbourne, Australia, 2019* (JACoW, Geneva, Switzerland, 2019), pp. 1698–1701.

[27] M. Ferrario *et al.*, Experimental Demonstration of Emittance Compensation with Velocity Bunching, Phys. Rev. Lett. **104**, 054801 (2010).

[28] J. Rosenzweig, *Fundamentals of Beam Physics* (Oxford University Press, Oxford, 2003).

[29] K. J. Kim, rf and space-charge effects in laser-driven rf electron guns, Nucl. Instrum. Methods Phys. Res., Sect. A **275**, 201 (1989).

[30] J. Rosenzweig and E. Colby, Charge and wavelength scaling of rf photoinjectors: A design tool, in *Proceedings of the Particle Accelerator Conference, Dallas, TX, 1995* (IEEE, New York, 1995), Vol. 2, pp. 957–960.

[31] B. O'Shea, J. Rosenzweig, A. Boni, A. Fukasawa, D. Alesini, M. Ferrario, B. Spataro, L. Ficcadenti, A. Mostacci, and L. Palumbo, rf design of theUCLA/INFN hybrid SW/TW photoinjector, AIP Conf. Proc. **877**, 873 (2006).

[32] B. O'Shea, A. Boni, A. Fukasawa, J. Rosenzweig, D. Alesini, M. Ferrario, B. Spataro, L. Ficcadenti, A. Mostacci, and L. Palumbo, Measurement of the UCLA/URLS/INFN hybrid gun, in *Proceedings of the 22nd Particle Accelerator Conference, PAC-2007, Albuquerque, NM* (IEEE, New York, 2007), pp. 2418–2420.

[33] A. Fukasawa, H. To, S. Mahapatra, B. Baumgartner, A. Cahill, K. Fitzmorris, R. Li, P. Musumeci, J. Rosenzweig, B. Spataro *et al.*, Progress on the hybrid gunproject at UCLA, Phys. Procedia **52**, 2 (2014).

[34] A. Fukasawa, J. Rosenzweig, A. Boni, B. O'Shea, D. Alesini, M. Ferrario, B. Spataro, L. Ficcadenti, A. Mostacci, and L. Palumbo, Charge and wavelength scaling of the UCLA/URLS/INFN hybrid photoinjector, in *Proceedings of the 22nd Particle Accelerator Conference, PAC-2007, Albuquerque, NM* (IEEE, New York, 2007), pp. 3609–3611.

[35] B. Spataro, A. Valloni, D. Alesini, N. Biancacci, L. Faillace, L. Ficcadenti, A. Fukusawa, L. Lancia, M. Migliorati, F. Morelli *et al.*, rf properties of a X-band hybrid photoinjector, Nucl. Instrum. Methods Phys. Res., Sect. A **657**, 99 (2011).

[36] J. Rosenzweig, A. Valloni, D. Alesini, G. Andonian, N. Bernard, L. Faillace, L. Ficcadenti, A. Fukusawa, B. Hidding, M. Migliorati *et al.*, Design and applications of an X-band hybrid photoinjector, Nucl. Instrum. Methods Phys. Res., Sect. A **657**, 107 (2011).

[37] L. Serafini and J. B. Rosenzweig, Envelope analysis of intense relativistic quasilaminar beams in rf photoinjectors: A theory of emittance compensation, Phys. Rev. E **55**, 7565 (1997).

[38] A. W. Chao, *Physics of Collective Beam Instabilities in High Energy Accelerators*, Wiley Series in Beam Physics and Accelerator Technology (Wiley-VCH, New York, 1993).

[39] L. Palumbo, V. G. Vaccaro, and M. Zobov, Wake fields and impedance, 10.15161/oar.it/1448441728.46 (1994).

[40] W. Panofsky and M. Bander, Asymptotic theory of beam break-up in linear accelerators, Rev. Sci. Instrum. **39**, 206 (1968).

[41] https://www.ansys.com/products/electronics/ansys-hfss.

[42] L. Faillace, F. Bosco, M. Carillo, L. Giuliano, M. Migliorati, A. Mostacci, L. Palumbo, A. Fukasawa, N. Majernik, O. Williams *et al.*, Beam dynamics for a high-field C-band hybrid photoinjector, in *Proceedings of the 12th International Particle Accelerator Conference, IPAC-2021, Campinas, SP, Brazil* (JACoW Publishing, Geneva, Switzerland, 2021).

[43] http://www.pulsar.nl/gpt/index.html.

[44] S. Tantawi, M. Nasr, Z. Li, C. Limborg, and P. Borchard, Distributed coupling accelerator structures: A new paradigm for high gradient linacs, arXiv:1811.09925.

[45] S. Hartman and J. Rosenzweig, Ponderomotive focusing in axisymmetric rf linacs, Phys. Rev. E **47**, 2031 (1993).

[46] F. Zhou, A. Brachmann, P. Emma, S. Gilevich, and Z. Huang, Impact of the spatial laser distribution on photocathode gun operation, Phys. Rev. ST Accel. Beams **15**, 090701 (2012).

[47] M. Gross, H. J. Qian, P. Boonpornprasert, Y. Chen, J. D. Good, H. Huck, I. Isaev, C. Koschitzki, M. Krasilnikov, S. Lal, X. Li *et al.*, Emittance reduction of rf photoinjector generated electron beams by transverse laser beam shaping, J. Phys. Conf. Ser. **1350**, 012046 (2019).

[48] W. W. Li, Z. G. He, and Q. K. Jia, Generation and measurement of sub-picosecond electron bunch in photocathode rf gun, Chin. Phys. C **37**, 127002 (2013).

[49] M. Ferrario, M. Migliorati, and L. Palumbo, Space charge effects, arXiv:1601.05214.

[50] J. Rosenzweig and L. Serafini, Transverse particle motion in radio-frequency linear accelerators, Phys. Rev. E **49**, 1599 (1994).

[51] O. D. Kellogg, *Foundations of Potential Theory* (Springer, New York, 1953).

[52] L. Serafini, The short bunch blow-out regime in rf photoinjectors, AIP Conf. Proc. **413**, 321 (1997).

[53] O. J. Luiten, S. B. van der Geer, M. J. de Loos, F. B. Kiewiet, and M. J. van der Wiel, How to Realize Uniform Three-Dimensional Ellipsoidal Electron Bunches, Phys. Rev. Lett. **93**, 094802 (2004).

[54] P. Musumeci, J. T. Moody, R. J. England, J. B. Rosenzweig, and T. Tran, Experimental Generation and Characterization of Uniformly Filled Ellipsoidal Electron-Beam Distributions, Phys. Rev. Lett. **100**, 244801 (2008).

[55] S. G. Anderson and J. B. Rosenzweig, Non equilibrium transverse motion and emittance growth in ultrarelativistic space-charge dominated beams, Phys. Rev. ST Accel. Beams **3**, 094201 (2000).

[56] L. B. Tuckerman, Inertia factors of ellipsoids for use in airship design, Report No. 210, 1925.

[57] F. Bosco, M. Behtouei, M. Carillo, L. Faillace, A. Giribono, L. Giuliano, M. Migliorati, A. Mostacci, L. Palumbo, J. Rosenzweig, B. Spataro, and C. Vaccarezza, Modeling short range wakefield effects in a High Gradient Linac, in *Proceedings of the 12th International Particle Accelerator Conference, IPAC-2021, Campinas, SP, Brazil* (JACoW Publishing, Geneva, Switzerland, 2021),

pp. 3185–3188, 10.18429/JACoW-IPAC2021-WEPAB 238.

[58] S. Tantawi, M. Nasr, Z. Li, C. Limborg, and P. Borchard, Design and demonstration of a distributed-coupling linear accelerator structure, Phys. Rev. Accel. Beams **23**, 092001 (2020).

[59] K. L. F. Bane, Short-range dipole wakefields in accelerating structures for the NLC, Report No. SLAC-PUB-9663, 2003.

[60] M. Migliorati and L. Palumbo, Multibunch and multiparticle simulation code with an alternative approach to wakefield effects, Phys. Rev. ST Accel. Beams **18**, 031001 (2015).

[61] M. Migliorati, S. Aumon, E. Koukovini-Platia, A. Huschauer, E. Métral, G. Sterbini, and N. Wang, Instability studies at the CERN proton synchrotron during transition crossing, Phys. Rev. Accel. Beams **21**, 120101 (2018).

[62] R. Ruland, Alignment considerations for the next linear collider, in *Proceedings of the Particle Accelerator Conference, Dallas, TX, 1995* (IEEE, New York, 1995), Vol. 3, pp. 2009–2013.

[63] M. Pedrozzi, SwissFEL injector conceptual design report, Accelerator test facility for SwissFEL, Paul Scherrer Institute (PSI) Report No. PSI–10-05, 2010.

[64] F. Löhl *et al.*, Status of SwissFEL, in *Proceedings of the 28th International Linear Accelerator Conference, LINAC-2016, East Lansing, MI, USA* (JACOW, Geneva, Switzerland, 2017), pp. 22–26.

[65] J. C. Sheppard, M. J. Lee, M. C. Ross, J. T. Seeman, R. F. Stiening, and M. D. Woodley, Beam steering in the SLC linac, IEEE Trans. Nucl. Sci. **32**, 2180 (1985).

[66] T. Raubenheimer and R. Ruth, A dispersion-free trajectory correction technique for linear colliders, Nucl. Instrum. Methods Phys. Res., Sect. A **302**, 191 (1991).

[67] A. M. Cook, R. Tikhoplav, S. Y. Tochitsky, G. Travish, O. B. Williams, and J. B. Rosenzweig, Observation of Narrow-Band Terahertz Coherent Cherenkov Radiation from a Cylindrical Dielectric-Lined Waveguide, Phys. Rev. Lett. **103**, 095003 (2009).

[68] J. K. Lim, P. Frigola, G. Travish, J. B. Rosenzweig, S. G. Anderson, W. J. Brown, J. S. Jacob, C. L. Robbins, and A. M. Tremaine, Adjustable, short focal length permanent-magnet quadrupole based electron beam final focus system, Phys. Rev. ST Accel. Beams **8**, 072401 (2005).

[69] F. Marteau, A. Ghaith, P. N'Gotta, C. Benabderrahmane, M. Valléau, C. Kitegi, A. Loulergue, J. Vétéran, M. Sebdaoui, T. André, G. Le Bec, J. Chavanne, C. Vallerand, D. Oumbarek, O. Cosson, F. Forest, P. Jivkov, J. L. Lancelot, and M. E. Couprie, Variable high gradient permanent magnet quadrupole (QUAPEVA), Appl. Phys. Lett. **111**, 253503 (2017).

[70] W. J. Brown and F. V. Hartemann, Three-dimensional time and frequency-domain theory of femtosecond x-ray pulse generation through Thomson scattering, Phys. Rev. ST Accel. Beams **7**, 060703 (2004).

[71] J. Rosenzweig and O. Williams, Limits on production of narrow band photons from inverse Compton scattering, AIP Conf. Proc. **877**, 437 (2006).

[72] A. Martens, F. Zomer, M. Amer, L. Amoudry, K. Cassou, K. Dupraz, and D. Nutarelli, Towards ultimate band-width photon sources based on Compton backscattering: Design constraints due to non-linear effects, Phys. Rev. Accel. Beams **24,** 091601 (2021).

[73] F. H. O'Shea, O. Williams, G. Andonian, S. Barber, Y. Sakai, J. B. Rosenzweig, I. Pogorelsky, M. Fedurin, K. Kusche, and V. Yakimenko, Single shot diffraction of picosecond 8.7-keV x-ray pulses, Phys. Rev. ST Accel. Beams **15,** 020702 (2012).

[74] http://genesis.web.psi.ch/index.html.